Received: 5 April 2021 | Revised: 8 June 2021 | Accepted: 15 June 2021

DOI: 10.1049/mia2.12172

IET Microwaves, Antennas & Propagation

The Institution of Engineering and Technology WILEY

ORIGINAL RESEARCH PAPER

Theoretical and numerical studies on multi-physical issues of space parabolic membrane antennas

Ming-Jian Li | Meng Li | Yu-Fei Liu | Cheng-Bo Cui

Qian Xuesen Laboratory of Space Technology, China Academy of Space Technology, Beijing, China

Correspondence

Meng Li, Qian Xuesen Laboratory of Space Technology, China Academy of Space Technology, Beijing 100094, China.
Email: limeng@qxslab.cn

Funding information

National Natural Science Foundation of China, Grant/Award Numbers: U1637207, U1937202, 52022075

Abstract

Front-fed parabolic reflectors are among the most commonly used antennas in the industry. While in spaceborne applications, membrane reflectors are very promising due to their lightweight and foldable features. However, considering the large size, small thickness and low stiffness, solar radiation and microwave radiation will have considerable influences on the antennas' shape accuracy as well as the radiation characteristics. In this article, a theoretical approach is presented to solve the multi-physical effects of the parabolic antenna. The deformation of the reflector is derived by the shallow shell theory, taking into account the solar pressure, the microwave pressure and the thermal effects due to solar and microwave heating. The far-field electromagnetic radiation pattern is then obtained by considering the deformation of the reflector. On the other hand, a numerical approach combining the finite element method, the multi-level fast multipole method, and the large element physical optics is also presented. Numerical examples suggest good agreement between the theoretical and numerical results. The methods have been applied into the analysis of design models in the Space Solar Power Station project. Also, these approaches can be directly extended into other space membrane reflector antennas.

1 | INTRODUCTION

Thin membrane antennas have been of great interest in the past few decades, owing to the increasing demand for large aperture space antennas [1–3]. The obvious merits of membrane antennas are their large sizes and light weights, since they can be folded into a small stowage volume and deployed on orbit. Typical deploying methods include inflation [4], elastic ribs-driven method [5, 6], Shape Memory Polymer-inflation[7, 8], and electrostatic forming [9, 10], and the antenna shapes after deployment are either parabolic or planar. Despite extensive studies in the United States [11], Europe [12], China [13], Japan [14] etc., practical applications in a spaceborne environment are still very rare. One example is the on-orbit experiment of a 14-m inflatable parabolic reflector [15–17], as a part of the In-Space Technology Experiments Program (IN-STEP). While on orbit, the deployment sequence did not materialise as planned due to the underestimation of residual gas and strain energy in the stowed structure, yet the torus and the struts completed deployment in another way. Another example is the very recently launched (2019) Radio Frequency Risk Reduction Deployment Demonstration (R3D2) satellite for the US Defense Advanced Research Projects Agency (DARPA) [18]. In this mission, a 2.25-m reflectarray antenna has been used. The membrane antenna is deployed by a frame structure instead of inflation. Up until now, the studies of membrane antennas have faced great challenges due to the difficulties in deploying, shape accuracy maintaining, and many other aspects.

The vision of harnessing solar power from space for terrestrial markets inspires continuous efforts in Space Solar Power Station (SSPS) projects [19–22]. Among these projects, the SSPS-OMEGA (Orb-Shape Membrane Energy Gathering Array) concept [23] is our focus, and in this project, a high-gain and large-aperture (100 m) antenna is one of its core components. The parabolic membrane antenna thus becomes a promising potential design. However, the large size and low stiffness feature of a membrane antenna makes it very sensitive to external forces. The coupling effects of the sunlight field, electromagnetic field, temperature field and the structural field thus become one of the most important issues in the antenna design and analysis work.

Investigations on multi-physical issues of antennas are mainly conducted by numerical simulations [24–28], and usually the surface distortion influence on radiation characteristics is the main concern. Zhang et al. [29] studied the microwave pressure on a parabolic antenna and the influence of shape distortion on the radiation pattern. Lu et al. [30] numerically investigated a large planar phased-array antenna in a space thermal environment, and introduced a shape adjustment method that utilises cables as actuators. Wang et al. [31] investigated coupled structural–electromagnetic relations of the planar rectangular active phased-array antennas and presented the combined influences of the radiated element numbers, mechanical distortion and element position random error on the antennas' electromagnetic performances. Guo et al. [32] presented finite element analysis on thermal–structural effects of the deployable AstroMesh antenna under extreme heat loads. Fan et al. [33] studied the influences of wrinkle distortion caused by tension cables on the electromagnetic performance of an active membrane phased-array antenna in P-band. Other studies can also provide useful references, such as studies on non-linear dynamics under thermal excitations [34, 35], the structure–electronic synthesis design [36], the deployment analysis of antennas [37], and multi-physical coupling effects in other regions [38–40].

The coupled studies of light, electromagnetic, temperature and structural fields are very rare in the literature. Among the current antenna studies, numerical simulation is the main approach. In this article, a theoretical solution to the coupled fields in parabolic antennas has been derived, and numerical simulations are also presented. The two approaches are in good agreement and can be used as a benchmark for future antenna analysis.

The remainder of the article is organised as follows: In Section 2, we present the theoretical solution to the reflector's deformation as well as the far-field pattern, during which process, the solar radiation, the microwave radiation and the thermal effects have been considered. In Section 3, the sequentialsolving numerical method is presented. Then, several practical cases have been solved based on the SSPS project. Good agreement between the theoretical and the numerical approaches has been achieved, and the effects of each field have been analysed. Conclusions are made in Section 4.

2 | THEORETICAL ANALYSIS

2.1 | Solar radiation on the antenna

A typical front-fed parabolic reflector antenna is shown in Figure 1. Two coordinate systems have been established at the centre of the reflector: the Cartesian system $Oxyz$ and the spherical system $Or\varphi\theta$. In $Oxyz$, the configuration equation of an ideal parabolic reflector is written as follows:

$$x^2 + y^2 = 4fz \tag{1}$$

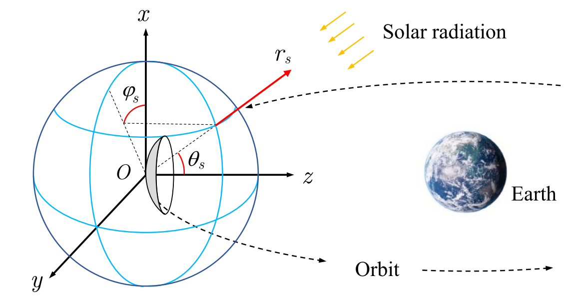

FIGURE 1 The Cartesian and spherical coordinate systems on the reflector antenna

where f is the focal length of the antenna. The radius of the projected antenna's circular aperture on the plane Oxy is defined as R. The unit normal vector on the reflector surface is denoted by $\boldsymbol{n}$ and can be obtained by taking the derivatives of Equation (1):

$$\boldsymbol{n} = \frac{1}{2\sqrt{f(z+f)}}\left(-x\hat{\boldsymbol{e}}_x - y\hat{\boldsymbol{e}}_y + 2f\hat{\boldsymbol{e}}_z\right) \tag{2}$$

The reflector receives solar radiation in space and deforms under its pressure. On defining the azimuth and altitude angles of the sun that are φ_s and θ_s, respectively, the unit vector $\boldsymbol{r}_s$ pointing to the sun is then as follows:

$$\boldsymbol{r}_s = \sin\theta_s \cos\varphi_s \hat{\boldsymbol{e}}_x + \sin\theta_s \sin\varphi_s \hat{\boldsymbol{e}}_y + \cos\theta_s \hat{\boldsymbol{e}}_z \tag{3}$$

where $\hat{\boldsymbol{e}}_x$, $\boldsymbol{e}_y$ and $\hat{\boldsymbol{e}}_z$ are base vectors in the Cartesian coordinate system $Oxyz$.

The total radiation power of the sun is known as $P_{sun} = 3.805 \times 10^{26}$ W, and its power density at the Earth is as follows:

$$W_e = \frac{P_{sun}}{4\pi L_e^2} \approx 1353\ \mathrm{W \cdot m^{-2}} \tag{4}$$

where L_e is the Earth–Sun distance. Since the orbit height of the antenna is negligible compared with the Earth–Sun distance, it is acceptable to regard the solar radiation power density W_e as uniform at any position of the orbit.

Despite the existence of complicated diffuse reflection and secondary reflection of the sunlight, let us simplify the solar power density as follows:

$$W_e = W_s + W_{sa} \tag{5}$$

where W_s in the solar power density reflected by the antenna, which leads to solar pressure, and W_{sa} is the solar power density absorbed by the antenna, which causes thermal deformation.

According to Einstein's theory of relativity, the energy E_p of a beam of photons can be expressed as $E_p = P_p c$, since photons have zero rest mass. Here, P_p denotes the momentum of photons and c is the speed of light. On a small area $\mathrm{d}A$ of the antenna, the solar energy reflected within time $\mathrm{d}t$ is $\mathrm{d}E_\mathrm{p} = W_\mathrm{s}\mathrm{d}t\ \mathrm{d}A$. Considering the momentum change of photons to be $\mathrm{d}P_\mathrm{p} = \mathrm{d}E_\mathrm{p}/c$, the solar pressure per area is then obtained by the momentum theorem as $\mathrm{d}P_\mathrm{p}/(\mathrm{d}t\ \mathrm{d}A) = W_\mathrm{s}/c$. For a specular reflection case, taking into account the momentum of incoming and reflected light, the solar pressure p_s will be as follows:

$$p_\mathrm{s} = -2\frac{W_\mathrm{s}}{c}\cos^2\beta_\mathrm{s} \tag{6}$$

where β_s is the incident angle of light beams (see Figure 2) and is expressed by the following:

$$\cos\beta_\mathrm{s} = \boldsymbol{r}_\mathrm{s}\cdot\boldsymbol{n} = \frac{-x\sin\theta_\mathrm{s}\cos\varphi_\mathrm{s} - y\sin\theta_\mathrm{s}\sin\varphi_\mathrm{s} + 2f\cos\theta_\mathrm{s}}{\sqrt{x^2+y^2+4f^2}} \tag{7}$$

where $\boldsymbol{r}_\mathrm{s}$ is in Equation (3) and $\boldsymbol{n}$ is in Equation (2).

Equation (6) only considers the sunlight coming in from the front of the antenna. To take into account the direction of the solar pressure, we can rewrite Equation (6) into the following form:

$$p_\mathrm{s} = -2\frac{W_\mathrm{s}}{c}\cos^2\beta_\mathrm{s}\tanh(\zeta\cos\beta_\mathrm{s}) \tag{8}$$

The hyperbolic tangent function introduced here is to distinguish the direction of the pressure. A tunable coefficient ζ has been introduced here to control the steepness of the hyperbolic tangent function. Typically, given $\zeta \geq 100$, the hyperbolic function is very similar to the sign function. Unlike the sign function, this function is differentiable and is convenient for the following derivation: The solar pressure satisfies $p_\mathrm{s} < 0$ when $\beta_\mathrm{s} \in (0, \pi/2)$ and $p_\mathrm{s} > 0$ when $\beta_\mathrm{s} \in (\pi/2, \pi)$. This means Equation (8) can describe the sunlight from the front as well as from the back of the antenna, in a unified formulation.

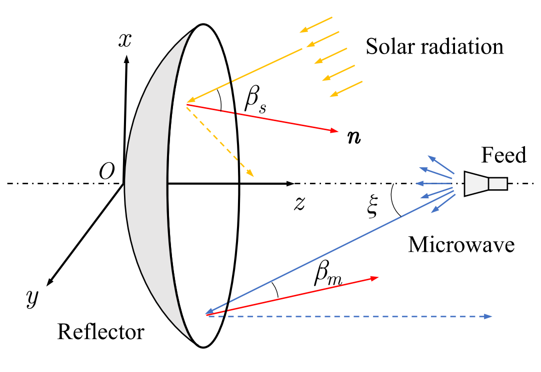

FIGURE 2 Sunlight pressure and microwave pressure on the reflector antenna

2.2 | Electromagnetic radiation on the antenna

The antenna is also illuminated by the electromagnetic wave from the feed (see Figure 2). The penetration depth of the wave is expressed as the skin depth.

$$\delta_\mathrm{m} = \sqrt{2/(\omega\mu_\mathrm{m}\sigma_\mathrm{m})}$$

where ω is the angular frequency of the electromagnetic wave, μ_m is the magnetic permeability, and σ_m is the electric conductivity. In the scope of this article, δ_m is negligible due to the high frequency of the incoming microwave. For a typical antenna with a polyimide base layer and a metal layer, the skin depth of the metal layer is usually of micron order. Therefore, the microwave radiation pressure can be regarded as the surface load on the reflector.

The feed of the parabolic reflector is usually a horn antenna and its radiation pattern is as follows:

$$F(\xi) = \cos^q\xi \tag{9}$$

where q is a constant coefficient and ξ is the angle between the radiation path and the z-axis (Figure 2). On defining the maximum microwave power density from the feed to be W_mx, it can be divided into the following:

$$W_\mathrm{mx} = W_\mathrm{m} + W_\mathrm{ma} \tag{10}$$

where W_m in the maximum power density reflected by the antenna, which is the major part and leads to the microwave pressure on the antenna. W_ma is the maximum power density absorbed by the antenna, which causes thermal deformation.

Similar to Equation (6), the microwave radiation pressure is written as follows:

$$p_\mathrm{m} = -2\frac{W_\mathrm{m}}{c}\cos^{2q}\xi\cos^2\beta_\mathrm{m} \tag{11}$$

where β_m is the incident angle of the radiation (see Figure 2). The angles can be easily obtained by means of the geometric relations and are written as follows:

$$\cos\xi = \frac{f-z}{f+z}, \quad \cos^2\beta_\mathrm{m} = \frac{f}{f+z} \tag{12}$$

Unlike the solar pressure in Equation (8), the direction of the microwave remains unchanged and p_m is always negative. The microwave pressure is finally the following:

$$p_\mathrm{m} = -2\frac{W_\mathrm{m}}{c}\frac{f(f-z)^{2q}}{(f+z)^{2q+1}} \tag{13}$$

From the above analysis, the total pressure p on the reflector surface becomes the combination of the solar pressure and the microwave pressure:

$$p = p_s + p_m \tag{14}$$

2.3 | The antenna's temperature affected by solar and microwave radiation

The reflector receives heat from the solar and microwave radiation and it also radiates heat into space. The microwave heating power density remains unchanged during operation, while the solar heating varies due to the changing incident angle and the blockage of the Earth. The current temperature is defined as T_1 in the reflector, while the reference (initial) temperature is T_0. Hence, the following equation is satisfied:

$$W_{sa}\cos\beta_s + W_{ma}\cos^{2q}\xi\cos\beta_m - \sigma_T(\eta_1+\eta_2)T_1^4 = \kappa\frac{\partial T_1}{\partial n} \tag{15}$$

where κ is the thermal conductivity, η_1 and η_2 are emissivity of the upper and lower surfaces, and $\sigma_T = 5.67\times10^{-8}\ \mathrm{W/m^2/K^4}$ is the Stefan–Boltzmann constant. The first term in Equation (15) expresses the heat flux absorbed from the microwave, the second term is the solar heating, and the third term is the heat lost into space. Due to the very small thickness of the reflector, T_1 can be treated as uniform along the z-direction, and the right-hand-side term in Equation (15) is then zero. Assuming the temperature change to be $T = T_1 - T_0$, it hence meets the following:

$$T = \left[\frac{W_{sa}\cos\beta_s + W_{ma}\cos^{2q}\xi\cos\beta_m}{\sigma_T(\eta_1+\eta_2)}\right]^{\frac{1}{4}} - T_0 \tag{16}$$

2.4 | The antenna's deformation in the light and electromagnetic fields

Due to a small sag–diameter ratio for a typical antenna (far less than 0.2), the problem arises with achieving the solution to a shallow thin shell's deformation under the non-axisymmetric pressure p and the temperature change T.

We take the assumptions of linear elastic, isotropic, small deformation and no pre-stresses. Then, by using the non-moment theory of thin shells, we first have the equations of geometry as follows:

$$\begin{cases}\varepsilon_x = \dfrac{\partial u}{\partial x} + \dfrac{1}{2f}w + \alpha T\\[2mm] \varepsilon_y = \dfrac{\partial v}{\partial y} + \dfrac{1}{2f}w + \alpha T\\[2mm] \varepsilon_{xy} = \dfrac{\partial u}{\partial y} + \dfrac{\partial v}{\partial x}\end{cases} \tag{17}$$

where u, v, w are the x-, y- and z-displacements, and ε_x, ε_y and ε_{xy} are strains. $1/(2f)$ is the curvature and α is the coefficient of linear thermal expansion.

The equations of physics are as follows:

$$\begin{cases}N_x = \dfrac{Eh}{1-\mu^2}(\varepsilon_x + \mu\varepsilon_y)\\[2mm] N_y = \dfrac{Eh}{1-\mu^2}(\varepsilon_y + \mu\varepsilon_x)\\[2mm] N_{xy} = \dfrac{Eh}{2(1+\mu)}\varepsilon_{xy}\end{cases} \tag{18}$$

where E, μ and h are the Young's modulus, the Poisson's ratio and the thickness of the shell, respectively. N_x, N_y and N_{xy} are internal forces.

The equations of equilibrium are as follows:

$$\begin{cases}\dfrac{\partial N_x}{\partial x} + \dfrac{\partial N_{xy}}{\partial y} = 0\\[2mm] \dfrac{\partial N_y}{\partial y} + \dfrac{\partial N_{xy}}{\partial x} = 0\\[2mm] \dfrac{1}{2f}(N_x + N_y) = p\end{cases} \tag{19}$$

By substituting Equation (17) into Equation (18) and then by substituting Equation (18) into Equation (19), we will get the displacement differential equations:

$$\begin{cases}2\dfrac{\partial^2 u}{\partial x^2} + (1-\mu)\dfrac{\partial^2 u}{\partial y^2} + (1+\mu)\dfrac{\partial^2 v}{\partial x\,\partial y} + \dfrac{1}{f}(1+\mu)\dfrac{\partial w}{\partial x} = -2(1+\mu)\alpha\dfrac{\partial T}{\partial x} & (20)\\[2mm] 2\dfrac{\partial^2 v}{\partial y^2} + (1-\mu)\dfrac{\partial^2 v}{\partial x^2} + (1+\mu)\dfrac{\partial^2 u}{\partial x\,\partial y} + \dfrac{1}{f}(1+\mu)\dfrac{\partial w}{\partial y} = -2(1+\mu)\alpha\dfrac{\partial T}{\partial y} & (21)\\[2mm] \dfrac{Eh}{1-\mu}\dfrac{1}{2f}\left(\dfrac{\partial u}{\partial x} + \dfrac{\partial v}{\partial y} + \dfrac{1}{f}w\right) = p - \dfrac{Eh\alpha T}{f(1-\mu)} & (22)\end{cases}$$

For the simply supported edge, the boundary conditions are as follows:

$$u|_{\varrho=R} = 0,\quad v|_{\varrho=R} = 0,\quad w|_{\varrho=R} = 0 \tag{23}$$

where $\varrho = \sqrt{x^2+y^2}$ is the radial coordinate.

By taking the partial derivatives to Equation (22) with respect to x and y and by multiplying them by $(1+\mu)$ and substracting them by Equations (20) and (21), we will get the following:

$$\begin{cases}\dfrac{\partial^2 u}{\partial x^2} + \dfrac{\partial^2 u}{\partial y^2} = -\dfrac{2f(1+\mu)}{Eh}\dfrac{\partial p}{\partial x}\\[2mm] \dfrac{\partial^2 v}{\partial x^2} + \dfrac{\partial^2 v}{\partial y^2} = -\dfrac{2f(1+\mu)}{Eh}\dfrac{\partial p}{\partial y}\end{cases} \tag{24}$$

By using Taylor's expansion at (0, 0) to the right-hand sides of Equation (24), and keeping only linear terms, Equation (24) can be rewritten as follows:

$$\begin{cases} \nabla^2 u = -\dfrac{2f(1+\mu)}{Eh}(g_1 + g_2 x + g_3 y) & (25) \\ \nabla^2 v = -\dfrac{2f(1+\mu)}{Eh}(g_4 + g_5 x + g_6 y) & (26) \end{cases}$$

where

$$\begin{aligned} g_1 &= \frac{\partial p(0,0)}{\partial x}, \quad g_2 = \frac{\partial^2 p(0,0)}{\partial x^2}, \quad g_3 = \frac{\partial^2 p(0,0)}{\partial x \partial y} \\ g_4 &= \frac{\partial p(0,0)}{\partial y}, \quad g_5 = \frac{\partial^2 p(0,0)}{\partial y \partial x}, \quad g_6 = \frac{\partial^2 p(0,0)}{\partial y^2} \end{aligned} \tag{27}$$

In order to get u and v, the Poisson's equations (25) and (26) need to be solved. u can be divided into the following:

$$u = \bar{u} + u^* \tag{28}$$

where u^* is a special solution to Equation (25) as follows:

$$u^* = -\frac{2f(1+\mu)}{Eh}\left(\frac{1}{4}g_1 x^2 + \frac{1}{4}g_1 y^2 + \frac{1}{6}g_2 x^3 + \frac{1}{6}g_3 y^3\right) \tag{29}$$

and $\bar{u}$ meets the following:

$$\begin{cases} \nabla^2 \bar{u} = 0 \\ \bar{u}|_{\varrho=R} = -u^*|_{\varrho=R} \end{cases} \tag{30}$$

The solution to Equation (30) in the polar coordinate system $O\varrho\vartheta$ is as follows:

$$\begin{aligned} \bar{u}(\varrho,\vartheta) = C_0 + D_0 \ln\varrho + \sum_{m=1}^{\infty} \varrho^m (A_m \cos m\vartheta + B_m \sin m\vartheta) \\ + \sum_{m=1}^{\infty} \varrho^{-m} (C_m \cos m\vartheta + D_m \sin m\vartheta) \end{aligned} \tag{31}$$

On substituting the boundary condition in Equation (30) into Equation (31) and on comparing coefficients, the x-displacement is obtained as follows:

$$u = -\frac{f(1+\mu)}{4Eh}\left(x^2 + y^2 - R^2\right)(2g_1 + g_2 x + g_3 y) \tag{32}$$

Similarly, the y-displacement is as follows:

$$v = -\frac{f(1+\mu)}{4Eh}\left(x^2 + y^2 - R^2\right)(2g_3 + g_4 x + g_5 y) \tag{33}$$

On substituting Equations (32) and (33) into Equation (22), the z-displacement is finally the following:

$$\begin{aligned} w = \frac{2f^2(1-\mu)}{Eh}p + \frac{f^2(1+\mu)}{4Eh}\big[(3g_2 + g_6)x^2 \\ + (g_2 + 3g_6)y^2 + (2g_3 + 2g_5)xy + 4g_1 x \\ + 4g_4 y - (g_2 + g_6)R^2\big] - 2f\alpha T \end{aligned} \tag{34}$$

where $g_1 \sim g_6$ are given in Appendix A.

2.5 | Radiation pattern of the deformed antenna

The far electrical field of an ideal parabolic reflector can be derived by the aperture plane method, using Fourier's transform. In Figure 3, the deformation w obtained above needs to be taking into account. Since the z-displacement is the main concern here, and its major influence to the radiation characteristics is through the phase change, the far electrical field considering the reflector's deformation is then written as follows:

$$\begin{aligned} E_f(\theta_f,\varphi_f) = \int_0^{2\pi}\int_0^R E_0(\rho_a,\phi_a)\cdot\exp[\mathrm{j}(\varphi_s + \varphi_r)] \\ \cdot \exp\left[\mathrm{j}k\rho_a \sin\theta_f \cos(\varphi_f - \phi_a)\right]\rho_a \mathrm{d}\rho_a \mathrm{d}\phi_a \end{aligned} \tag{35}$$

where $k = 2\pi/\lambda$ and λ is the wave length. E_0 satisfies the following:

$$E_0(\rho_a,\phi_a) = \frac{F(\xi,\phi_a)}{r_0} \tag{36}$$

where F is the radiation pattern of the feed given in Equation (9). $r_0 = z + f$ is the distance of the radiation path. On substituting Equations (12) and (9) into Equation (36) and then transforming it to the polar coordinate system, we will get the following:

$$E_0(\rho_a,\phi_a) = \frac{4f\left(4f^2 - \rho_a^2\right)^q}{\left(4f^2 + \rho_a^2\right)^{q+1}} \tag{37}$$

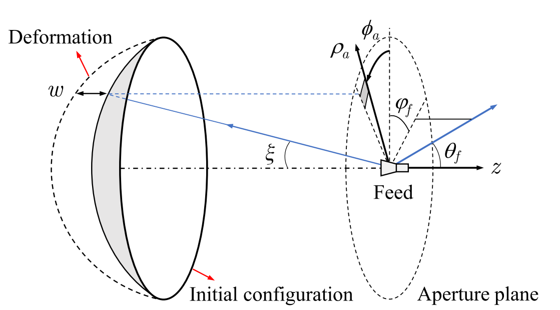

FIGURE 3 The deformation of the antenna and its influence on the radiation path error

The system error and random error are denoted by φ_s and φ_r, respectively, in Equation (35). Here, we only consider the influence of the antenna's deformation w; thus,

$$\varphi_s + \varphi_r \approx \varphi_s = kw(1 + \cos\xi) \tag{38}$$

On substituting Equations (38) and (34) into Equation (35), the electrical field change caused by the antenna's deformation will be obtained. To be noted, due to its complexity, Equation (35) can be numerically achieved by quadrature methods.

3 | NUMERICAL APPROACH AND APPLICATIONS

3.1 | Numerical methodology

The numerical simulation is based on a sequential solving framework, which has been presented in Figure 4. First, the solar radiation pressure, the microwave pressure, and the temperature variation are obtained by the above mentioned equations. Then, in order to solve the deformation of the reflector, the finite element method (FEM) is applied and 8-node membrane elements are used. The pressure p is applied as surface loads on the elements and the temperature change T is applied as body loads. The edge is simply supported, which means all three translational degrees of freedom are fixed.

The deformation of the reflector will be solved by ANSYS Mechanical, once w is obtained on the structural grids. It will be interpolated to the electromagnetic grids and will be solved by FEKO afterwards.

In order to solve the high-frequency electromagnetic problem, the radiation pattern of the feed is first simulated. The multi-level fast multipole method (MLFMM) is used to deal with the feed, with good efficiency and accuracy. Since the reflector is electrically large, the large element physical optics (LEPO) method [41, 42] is then used to solve the reflector. The coupling effects are considered by iterative methods between the MLFMM and LEPO solutions.

3.2 | The space membrane antenna model

As applications to the theoretical and numerical approaches above, let us consider several practical cases. These cases are based on the SSPS project; however, the methods can be extended to any space parabolic membrane antennas under similar working conditions.

The model is a parabolic membrane reflector antenna with a horn feed (Figure 5). The radius of the reflector is $R = 7$ m, the focal length is $f = 2R$, and the thickness is $h = 10$ μm. Kapton is used as the base material of the reflector; it has a Young's modulus of 2.5 GPa, a Poisson's ratio of 0.3, and a coefficient of thermal expansion

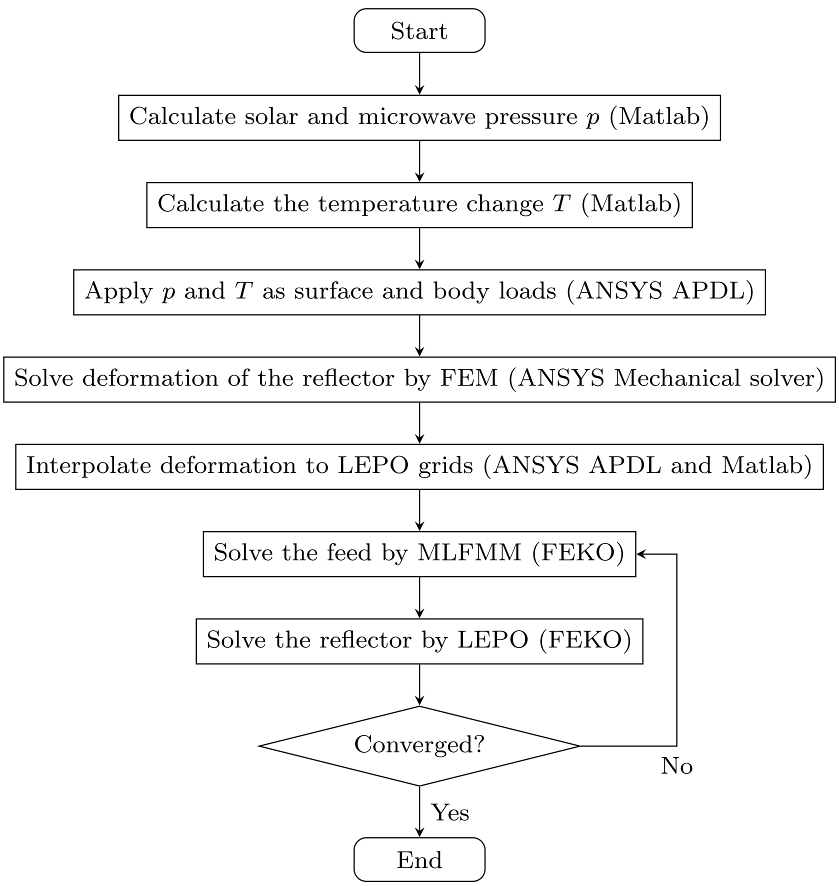

FIGURE 4 The numerical simulation process of the coupled system

$\alpha = 2 \times 10^{-5}$ K^{-1}. The emissivity of heat radiation is 0.9. The absorbed solar power density is $W_{sa} = 13.5$ W/m^2, which is about 1%W_e. The maximum microwave power density is $W_m = 1$ MW/m^2 and the absorbed microwave power density is $W_{ma} = 10$ W/m^2.

The feed is a conical horn antenna, and it works at the frequency 5.8 GHz. Its waveguide has a radius of 0.51λ and a length of 2.2λ. The horn's top and base radii are λ and 0.65λ, respectively, and its length is 3.05λ. The horn is discretised into about 15,000 grids (Figure 5). The directivity calculated has been presented in Figure 6. In theoretical approach, when $q = 6.5$, Equation (9) provides a result that is very similar to that of the numerical simulation.

Both the combined solar and microwave pressure p and the temperature change T are applied on the structural model. A total number of 6400 membrane elements are used in the FEM solution process. Considering the incident angles $\varphi_s = 0$ and $\theta_s = 0.4\pi$, the deformed shape of the reflector is as given in Figure 7, and the deformation w is given as contours in Figure 8. It can be seen that the theoretical solution is in line with the numerical result. The maximum theoretical displacement is 0.061 m and the maximum numerical displacement is 0.064 m. The relative error between the two methods is 4.7%.

The normalised radiation pattern is shown in Figure 9. As can be seen, in the ideal undeformed case, the theoretical and the numerical results are very close. For the deformed reflector, the theoretical and the numerical methods also provide very similar results on the main lobe, while for the side lobes, slight differences can be found. The differences may come from the approximation of the theory as well as the numerical model errors. However, this kind of difference is totally acceptable.

Figure 10 compares the directivities of the antenna before and after deformation. The gain decreases by 6.8 dB and the beam width also increases. The radiation characteristics considerably deteriorate. This means that the multi-physical issues must be taken into account in the design process of the space membrane antenna.

3.3 | Solar pressure influences

In order to investigate the influence of each contributor, let us first consider the solar pressure. Assuming the thickness $h = 5$ μm, the radius $R = 50$ m, and incident angles $\varphi_s = 0$, $\theta_s = 0.3\pi$, the deformation of the reflector is as shown in Figure 11. The relative error of the central point displacement is 2% and the relative error of the maximum displacement is 16% between the theoretical and numerical results. The differences may come from both the theoretical assumptions and the FEM errors for very thin structures. Assuming $\varphi_s = 0$, $\theta_s = 0, 0.05\pi, 0.1\pi, 0.2\pi, 0.3\pi, 0.4\pi$, the deformations are as shown in Figure 12. As can be seen, the theoretical and numerical results agree well. Also, the deflection tends to be larger when the incident angle is smaller. The solar pressure is of μPa order and contributes μm order deformation, even for a very large antenna. In the $R = 7$ m case, the deformation is even smaller and the radiation pattern will not be affected much by the solar pressure alone.

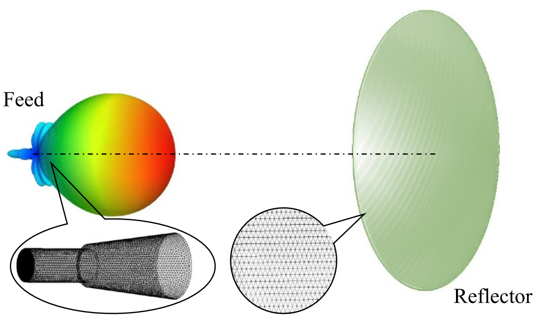

FIGURE 5 The mesh of the horn feed and the reflector

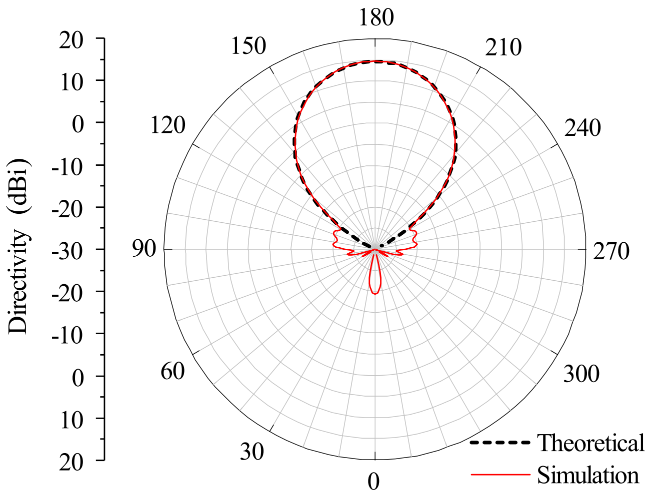

FIGURE 6 Directivity of the feed: comparison between the theoretical equation (9) with $q = 6.5$ and the numerical simulation of a conical horn antenna

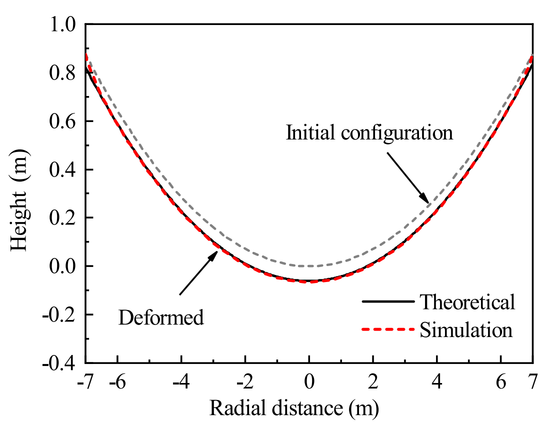

FIGURE 7 The deflection of the reflector under solar pressure with an incident angle 0.3π; the theoretical result and the simulation are in good agreement

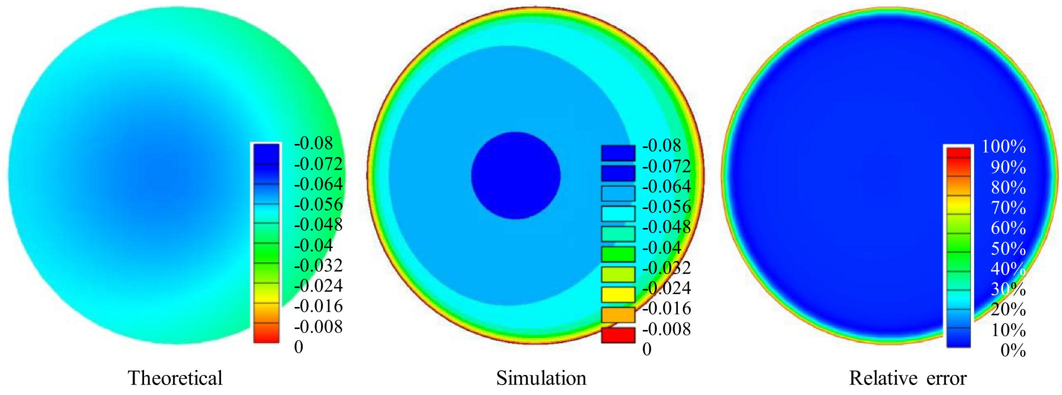

FIGURE 8 Contours of the displacement w, the theoretical distribution, the numerical results and the relative error

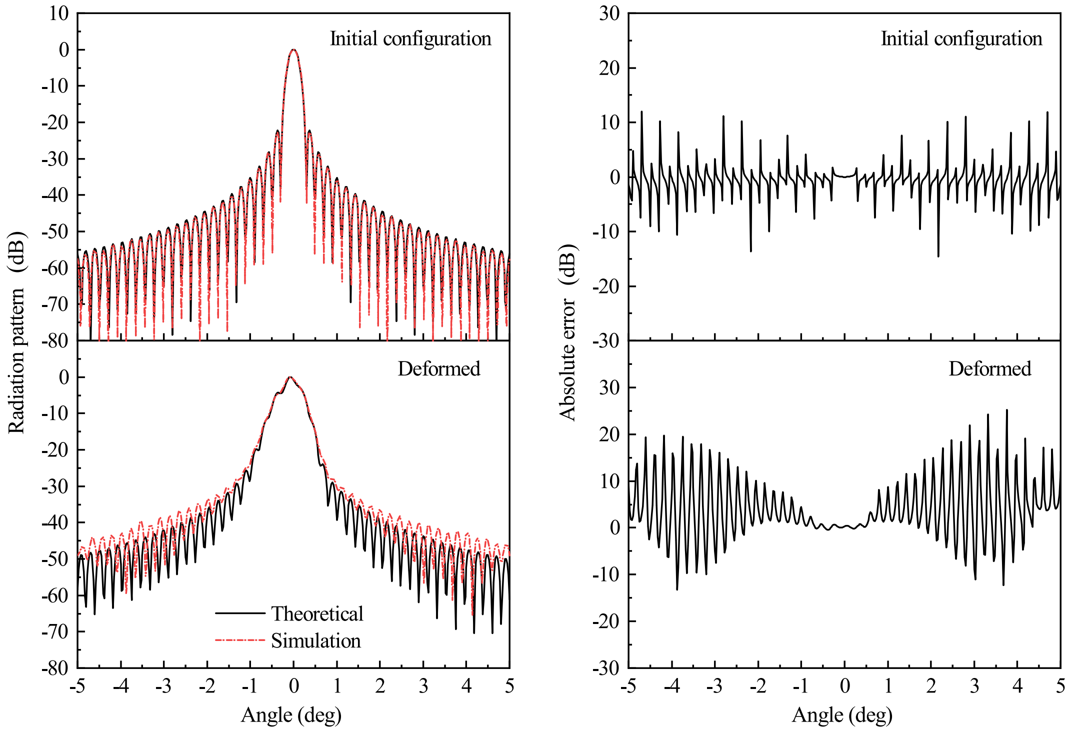

FIGURE 9 The theoretical and the numerical radiation patterns of the reflector. Absolute error between the two methods are presented. The side-lobe error is large because phase difference exists. Considering the maximum side-lobe level, the error is less than 5 dB

3.4 | The microwave pressure influences

Let us now consider only the microwave pressure. For $W_m = 1$ MW/m^2, the microwave pressure is of mPa order. Assuming the thickness $h = 5$ μm, the radius $R = 50$ m, and $q = 1$, the deformation of the reflector is then as shown in Figure 13 and the relative error of the maximum displacement is 3.6% between the theoretical and numerical results. The radiation pattern of the reflector is shown in Figure 14. As can be seen, for large and thin membranes, the microwave pressure can lead to considerable shape distortion and radiation pattern variation. In the SSPS project, microwave power density can be very large; thus, the microwave pressure effects needs to be considered under certain circumstances. Actually, the thermal deformation is the most important factor here, and the temperature is affected by solar and microwave heating. Typically, considering a high reflectivity in this article, the temperature of the reflector will reach 85 K under only solar radiation and will reach 105 K under microwave heating. When the reflectivity is smaller, the temperature will be much higher, and this means a careful temperature-control design is very necessary in the current antenna design work.

4 | CONCLUSION

In this article, we have presented a theoretical approach as well as a numerical approach to solve the multi-physical problem in space membrane parabolic reflector antennas. The light field,

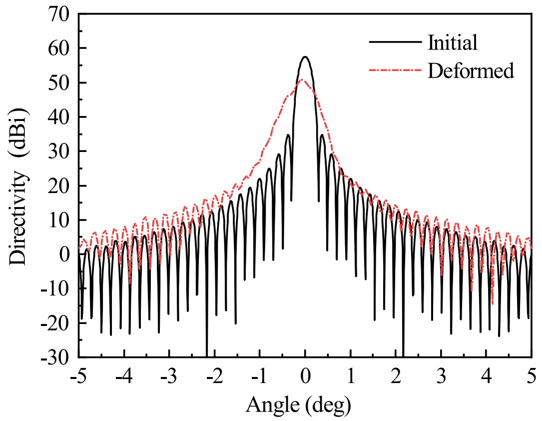

FIGURE 10 Directivities of the reflector before and after deformation

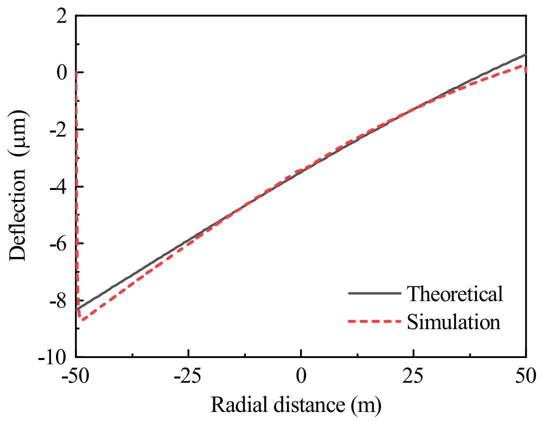

FIGURE 11 The deflection of the reflector with a radius 50 m under solar pressure with an incident angle 0.3π; the theoretical result and the simulation are in good agreement

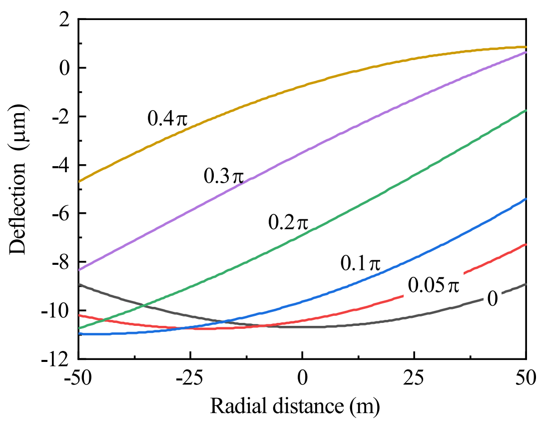

FIGURE 12 Deflections of the reflector under solar pressure with different incident angles: 0, 0.05π, 0.1π, 0.2π, 0.3π and 0.4π

electromagnetic field, temperature field and structural field are coupled as shown in Figure 15. Solar radiation leads to both pressure and heating, and thus structural deformation. Microwave radiation also causes pressure and thermal effects, and

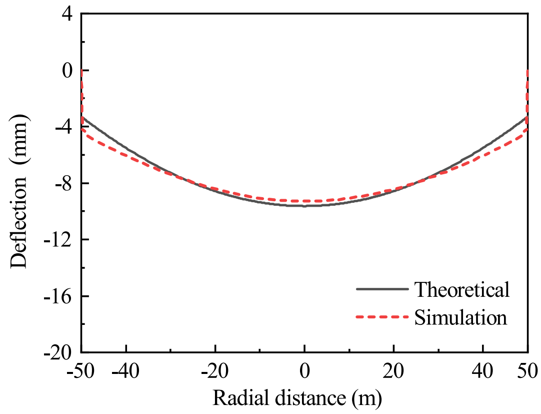

FIGURE 13 The deflection of the reflector with a radius 50 m under microwave pressure with $W_m = 1$ MW/m^2 and $q = 1$; the theoretical result and the simulation are in good agreement

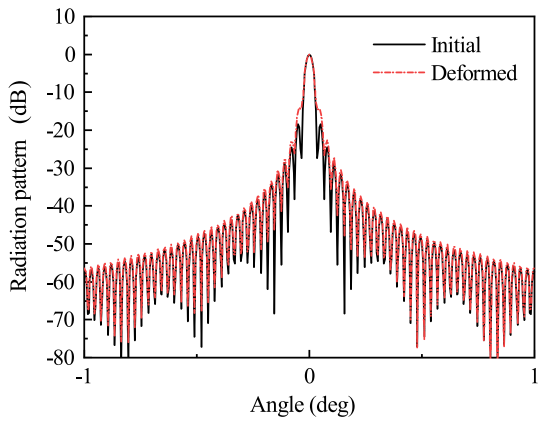

FIGURE 14 The radiation pattern of the reflector with a radius 50 m under microwave pressure with $W_m = 1$ MW/m^2 and $q = 1$

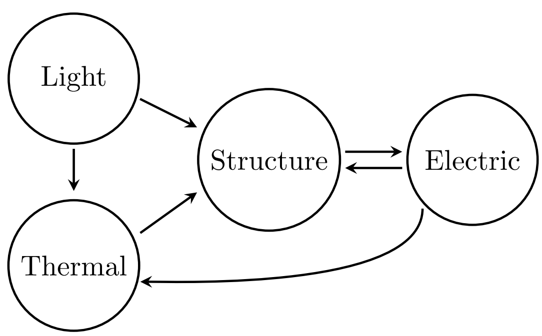

FIGURE 15 The coupling of multi-physical fields

directly and indirectly affects the structure. The structural deformation finally changes the electromagnetic radiation characteristics.

As applications of the methods above, membrane antennas in the SSPS project have been analysed. Results suggest good agreement between the theoretical and the numerical solutions. In these cases, the thermal effects of solar and microwave heating contribute the most to the structural deformation and radiation pattern deterioration. The microwave pressure also leads to considerable deformation, while the influence of the solar pressure is minimal.

The theoretical solution can be used as a benchmark for validation and verification purpose of future numerical methods. Both the theoretical and numerical approaches in this article can be extended into other space parabolic reflector studies, considering the coupling effects of light, temperature, electromagnetic, and structural fields.

ACKNOWLEDGEMENT

The authors acknowledge the support from the National Natural Science Foundation of China, under Grant No. U1637207, U1937202 and 52022075.

ORCID

Meng Li https://orcid.org/0000-0001-6570-6467

REFERENCES

1. Duan, B., Zhang, Y., Du, J.: Large Deployable Satellite Antennas: Design Theory, Methods and Applications. Springer Nature (2020)
2. Duan, B.: Large spaceborne deployable antennas (LSDAS) – a comprehensive summary. Chin. J. Electron. 29(1), 1–15 (2020)
3. Liu, Z.-Q., et al.: Review of large spacecraft deployable membrane antenna structures. Chin. J. Mech. Eng. 30(6), 1447–1459 (2017)
4. Stutzman, W.: Antennas and propagation in communication systems: past, present, and future. In: IEEE International Symposium on Antennas and Propagation (APSURSI), pp. 683–684. (2016). https://doi.org/10.1109/APS.2016.7696050
5. Dewalque, F., Collette, J.-P., Brüls, O.: Mechanical behaviour of tape springs used in the deployment of reflectors around a solar panel. Acta Astronaut. 123, 271–282 (2016)
6. Miyazaki, Y., Fukunaga, M., Kousaka, D.: Membrane structure supported by self-deployable truss for space applications. In: AIAA Spacecraft Structures Conference, p. 1201. (2018)
7. Liu, Y., et al.: Shape memory polymers and their composites in aerospace applications: a review. Smart Mater. Struct. 23(2), 023001 (2014)
8. Jape, S., et al.: Self-foldable origami reflector antenna enabled by shape memory polymer actuation. Smart Mater. Struct. 29(11), 115011 (2020)
9. Zhang, Y., et al.: Electrode grouping optimization of electrostatic forming membrane reflector antennas. Aero. Sci. Technol. 41, 158–166 (2015)
10. Liu, C., Shi, Y.: Comprehensive structural analysis and optimization of the electrostatic forming membrane reflector deployable antenna. Aero. Sci. Technol. 53, 267–279 (2016)
11. Pearson, J., Romanofsky, R.: Thin film antenna development and optimization. In: 47th AIAA/ASME/ASCE/AHS/ASC Structures, Structural Dynamics, and Materials Conference; 14th AIAA/ASME/AHS Adaptive Structures Conference, p. 2229 (2006)
12. Angevain, J.-C., et al.: Large deployable spaceborne reflector antennas in Europe: progress status and perspectives. In: 2019 13th European Conference on Antennas and Propagation (EuCAP), pp. 1–5. IEEE (2019)
13. Huang, J.: Paper-thin membrane aperture-coupled L-band antennas. IEEE Trans. Antenn. Propag. 53(8), 2499–2502 (2005). https://doi.org/10.1109/TAP.2005.852277
14. Shimoda, Y., et al.: Development of stereo camera system for accurate observation of deployable membranes onboard CubeSat. In: 55th AIAA Aerospace Sciences Meeting, p. 0167. (2017)
15. Freeland, R., Bilyeu, G., Veal, G.: Development of flight hardware for a large, inflatable-deployable antenna experiment. Acta Astronaut. 38(4–8), 251–260 (1996)
16. Freeland, R., et al.: Large inflatable deployable antenna flight experiment results. Acta Astronaut. 41(4–10), 267–277 (1997)
17. Freeland, R., Veal, G.: Significance of the inflatable antenna experiment technology. In: 39th AIAA/ASME/ASCE/AHS/ASC Structures, Structural Dynamics, and Materials Conference and Exhibit, pp. 2104. (1998)
18. De Zwart, M., Stephens, D.: The space (innovation) race: the inevitable relationship between military technology and innovation. Melb. J. Int. Law. 20, 1 (2019)
19. Mankins, J.C.: New directions for space solar power. Acta Astronaut. 65(1–2), 146–156 (2009)
20. Cheng, Z., et al.: In-orbit assembly mission for the space solar power station. Acta Astronaut. 129, 299–308 (2016)
21. Li, X., et al.: A new concept of space solar power satellite. Acta Astronaut. 136, 182–189 (2017)
22. Yermoldina, G., et al.: Features of space solar power station control system. Acta Astronaut. 158, 111–120 (2019)
23. Yang, Y., et al.: A novel design project for space solar power station (SSPS-OMEGA). Acta Astronaut. 121, 51–58 (2016)
24. Wang, C., et al.: Coupled structural–electromagnetic–thermal modelling and analysis of active phased array antennas. IET Microw. Antenn. Propag. 4(2), 247–257 (2010)
25. Song, L., et al.: Performance of planar slotted waveguide arrays with surface distortion. IEEE Trans. Antenn. Propag. 59(9), 3218–3223 (2011)
26. Lian, P., et al.: A pattern approximation method for distorted reflector antennas using piecewise linear fitting of the exponential error term. IEEE Trans. Antenn. Propag. 63(10), 4546–4551 (2015)
27. Duan, B., Qiao, H., Zeng, L.: The multi-field-coupled model and optimization of absorbing material's position and size of electronic equipments. J. Mechatron. Appl. 2010, 569529 (2010)
28. Duan, B.: Electromechanical Coupling Theory, Method and Application of Electronic Equipment. Science Press, Beijing (2011)
29. Zhang, X., et al.: Structural-electromagnetic bidirectional coupling analysis of space large film reflector antennas. Acta Astronaut. 139, 502–511 (2017)
30. Lu, G.-Y., et al.: Studies of thermal deformation and shape control of a space planar phased array antenna. Aero. Sci. Technol. 93, 105–311 (2019)
31. Wang, C., et al.: On the performance of array antennas with mechanical distortion errors considering element numbers. Int. J. Electron. 104(3), 462–484 (2017)
32. Guo, W., et al.: Thermal–structural analysis of large deployable space antenna under extreme heat loads. J. Therm. Stresses. 39(8), 887–905 (2016)
33. Fan, L., et al.: Coupled structural-electromagnetic modeling and analysis of active membrane phased array antenna. Adv. Space Res. 66(4), 760–770 (2020)
34. Zhang, W., Wu, R., Behdinan, K.: Nonlinear dynamic analysis near resonance of a beam-ring structure for modeling circular truss antenna under time-dependent thermal excitation. Aero. Sci. Technol. 86, 296–311 (2019)
35. Li, Y., Wang, C., Huang, W.: Rigid-flexible-thermal analysis of planar composite solar array with clearance joint considering torsional spring, latch mechanism and attitude controller. Nonlinear Dyn. 96(3), 2031–2053 (2019)
36. Xu, Y., Guan, F.-L.: Structure–electronic synthesis design of deployable truss antenna. Aero. Sci. Technol. 26(1), 259–267 (2013)
37. Zhang, Y., et al.: Deployment analysis considering the cable-net tension effect for deployable antennas. Aero. Sci. Technol. 48, 193–202 (2016)
38. Li, M.-J., Zhang, N.-M., Ni, M.-J.: Magneto-fluid-structure interaction issues for vibrating rigid bodies in conducting fluids: the numerical and the analytical approaches. Comput. Struct. 210, 41–57 (2018)
39. Bungartz, H.-J., et al.: preCICE – a fully parallel library for multi-physics surface coupling. Comput. Fluids. 141, 250–258 (2016)
40. Quarteroni, A., et al.: Integrated heart-coupling multiscale and multiphysics models for the simulation of the cardiac function. Comput. Methods Appl. Mech. Eng. 314, 345–407 (2017)
41. Taboada, J., et al.: Incorporation of linear-phase progression in RWG basis functions. Microw. Opt. Technol. Lett. 44(2), 106–112 (2005)

42. Nazo, S.: A Hybrid MoM/PO Technique with Large Element PO, Ph.D. thesis. Stellenbosch University, Stellenbosch (2012)

SUPPORTING INFORMATION

Additional supporting information may be found online in the Supporting Information section at the end of this article.

APPENDIX A

USEFUL EQUATIONS AND COEFFICIENTS

The complete form of the solar pressure is as follows, which can be obtained by substituting Equation (7) into Equation (6):

$$p_s = -2\frac{W_s}{c}\frac{(x\sin\theta_s\cos\varphi_s + y\sin\theta_s\sin\varphi_s - 2f\cos\theta_s)^2}{x^2+y^2+4f^2} \cdot \tanh\left(\zeta\frac{-x\sin\theta_s\cos\varphi_s - y\sin\theta_s\sin\varphi_s + 2f\cos\theta_s}{\sqrt{x^2+y^2+4f^2}}\right) \quad (A.1)$$

The Taylor's expansion to function $H(x, y)$ at (x_0, y_0) is as follows:

$$H(x,y) = \sum_{n=0}^{\infty}\frac{1}{n!}\left(x\frac{\partial}{\partial x} + y\frac{\partial}{\partial y}\right)^n H(x_0,y_0) \quad (A.2)$$

The coefficients $g_1 \sim g_6$ given in Equation (27) depend on a specific form of p. Assuming that the sunlight comes in from the front side of the reflector, Equation (6) is used to describe the solar pressure. $g_1 \sim g_6$ are then as follows:

$$g_1 = \frac{2W_s\cos\varphi_s\sin\theta_s\cos\theta_s}{cf} \quad (A.3)$$

$$g_2 = \frac{W_s(\cos^2\theta_s - \cos^2\varphi_s\sin^2\theta_s) + W_m(4q+1)}{cf^2} \quad (A.4)$$

$$g_3 = -\frac{W_s\sin\varphi_s\cos\varphi_s\sin^2\theta_s}{cf^2} \quad (A.5)$$

$$g_4 = \frac{2W_s\sin\varphi_s\sin\theta_s\cos\theta_s}{cf} \quad (A.6)$$

$$g_5 = g_3 \quad (A.7)$$

$$g_6 = \frac{W_s(\cos^2\theta_s - \sin^2\varphi_s\sin^2\theta_s) + W_m(4q+1)}{cf^2} \quad (A.8)$$

If the direction of the incoming sunlight is taken into account, Equation (8) will be used. $g_1 \sim g_6$ are then in the following forms:

$$g_1 = \frac{W_s}{cf}\cos\varphi_s\sin\theta_s\cos\theta_s\zeta\cos\theta_s + \sinh(2\zeta\cos\theta_s)\cdot\mathrm{sech}^2(\zeta\cos\theta_s) \quad (A.9)$$

$$g_2 = \frac{W_s}{2cf^2}\{2\tanh(\zeta\cos\theta_s)\cos^2\varphi_s\sin^2\theta_s\zeta^2\cos^2\theta_s \cdot \mathrm{sech}^2(\zeta\cos\theta_s) - 1 + \cos^2\theta_s + \zeta\cos\theta_s \cdot (\cos^2\theta_s - 4\cos^2\varphi_s\sin^2\theta_s)\mathrm{sech}^2(\zeta\cos\theta_s)\} + \frac{(4q+1)W_m}{cf^2} \quad (A.10)$$

$$g_3 = \frac{W_s}{cf^2}\sin\varphi_s\cos\varphi_s\sin^2\theta_s\{-\tanh(\zeta\cos\theta_s) + \zeta\cos\theta_s[\zeta\cos\theta_s\tanh(\zeta\cos\theta_s) - 2] \cdot \mathrm{sech}^2(\zeta\cos\theta_s)\} \quad (A.11)$$

$$g_4 = \frac{W_s}{cf}\sin\varphi_s\sin\theta_s\cos\theta_s\{\sinh(2\zeta\cos\theta_s) + \zeta\cos\theta_s\}\cdot\mathrm{sech}^2(\zeta\cos\theta_s) \quad (A.12)$$

$$g_5 = g_3 \quad (A.13)$$

$$g_6 = \frac{W_s}{2cf^2}\{2\tanh(\zeta\cos\theta_s)\sin^2\varphi_s\sin^2\theta_s\zeta^2\cos^2\theta_s \ \mathrm{sech}^2(\zeta\cos\theta_s) - 1 + \cos^2\theta_s + \zeta\cos\theta_s \cdot (\cos^2\theta_s - 4\sin^2\varphi_s\sin^2\theta_s)\mathrm{sech}^2(\zeta\cos\theta_s)\} + \frac{(4q+1)W_m}{cf^2} \quad (A.14)$$

In any circumstances, Equations (A.9)–(A.14) are suggested to be used, since they can deal with the sunlight coming in from the front as well as from the back of the reflector. However, when the angle satisfies $\theta_s < \arctan(4f/R) \approx 0.46\pi$, Equations (A.3)–(A.8) can be used for simplicity.

How to cite this article: Li, M.-J., et al.: Theoretical and numerical studies on multi-physical issues of space parabolic membrane antennas. IET Microw. Antennas Propag. 15(12), 1625–1635 (2021). https://doi.org/10.1049/mia2.12172